

First application of liquid-metal-jet sources for small-animal imaging: High-resolution CT and phase-contrast tumor demarcation

Daniel H. Larsson^{a)} and Ulf Lundström

Department of Applied Physics, KTH Royal Institute of Technology/Albanova, 10691 Stockholm, Sweden

Ulrica K. Westermark and Marie Arsenian Henriksson

Department of Microbiology, Tumor and Cell Biology (MTC), Karolinska Institutet, 17177 Stockholm, Sweden

Anna Burvall and Hans M. Hertz

Department of Applied Physics, KTH Royal Institute of Technology/Albanova, 10691 Stockholm, Sweden

(Received 26 September 2012; revised 22 December 2012; accepted for publication 3 January 2013; published 24 January 2013)

Purpose: Small-animal studies require images with high spatial resolution and high contrast due to the small scale of the structures. X-ray imaging systems for small animals are often limited by the microfocus source. Here, the authors investigate the applicability of liquid-metal-jet x-ray sources for such high-resolution small-animal imaging, both in tomography based on absorption and in soft-tissue tumor imaging based on in-line phase contrast.

Methods: The experimental arrangement consists of a liquid-metal-jet x-ray source, the small-animal object on a rotating stage, and an imaging detector. The source-to-object and object-to-detector distances are adjusted for the preferred contrast mechanism. Two different liquid-metal-jet sources are used, one circulating a Ga/In/Sn alloy and the other an In/Ga alloy for higher penetration through thick tissue. Both sources are operated at 40–50 W electron-beam power with $\sim 7 \mu\text{m}$ x-ray spots, providing high spatial resolution in absorption imaging and high spatial coherence for the phase-contrast imaging.

Results: High-resolution absorption imaging is demonstrated on mice with CT, showing $50 \mu\text{m}$ bone details in the reconstructed slices. High-resolution phase-contrast soft-tissue imaging shows clear demarcation of mm-sized tumors at much lower dose than is required in absorption.

Conclusions: This is the first application of liquid-metal-jet x-ray sources for whole-body small-animal x-ray imaging. In absorption, the method allows high-resolution tomographic skeletal imaging with potential for significantly shorter exposure times due to the power scalability of liquid-metal-jet sources. In phase contrast, the authors use a simple in-line arrangement to show distinct tumor demarcation of few-mm-sized tumors. This is, to their knowledge, the first small-animal tumor visualization with a laboratory phase-contrast system. © 2013 American Association of Physicists in Medicine. [<http://dx.doi.org/10.1118/1.4788661>]

Key words: small-animal imaging, liquid-metal-jet, x-ray, CT, tumor demarcation, mouse

I. INTRODUCTION

Whole-body small-animal imaging is extensively used in basic and preclinical medical research, e.g., in drug discovery and for understanding mechanisms of disease.^{1,2} X-ray computed tomography (CT) of small animals is an attractive modality since it can provide high spatial resolution with high throughput at relatively low cost.^{3,4} However, current small-animal imaging systems are typically constrained by the microfocus x-ray source. In the present paper, we demonstrate the first small-animal x-ray imaging using a novel source technology, the liquid-metal-jet x-ray source,^{5–7} which has potential to increase the power of high-resolution small-animal x-ray imaging by shortening exposure times and increasing the observable detail by use of phase contrast.

X-ray imaging of small animals requires much higher spatial resolution than clinical imaging due to the smaller scale of, e.g., organs and other structures. Spatial resolution is ultimately determined by the x-ray spot size of the source via the penumbral blurring (assuming the detector pixel size is suf-

ficiently small not to limit spatial resolution). Consequently, classical absorption imaging systems like small-animal CT scanners typically rely on microfocus sources. Furthermore, temporal resolution and exposure times are important, in particular when imaging living animals. Short exposure times require a high photon flux from the source, which in turn requires high electron-beam (e-beam) power. Finally, we note that photon energies in the range of a few tens of keV are necessary for penetration through a few cm of tissue, e.g., a mouse. In summary, high-resolution whole-body CT of small animals requires few-10-keV sources with small x-ray spots and sufficient power, e.g., sources with high e-beam power density. High-end commercial small-animal microfocus CT systems typically employ stationary targets with 1–10 μm spot sizes and 1–10 W e-beam power,^{1,2} roughly consistent with the reported thermal limitation of such targets⁸ of 0.4–0.8 W/ μm^2 which corresponds to an e-beam power density of 50–100 kW/mm² for a 10- μm source. The liquid-metal-jet x-ray source concept^{5–7} circumvents this thermal limitation by using a regenerative e-beam target to allow for a higher power

density and thereby a higher photon flux. Currently, liquid-metal-jet microfocus systems are commercially operated over extended periods at 600–1300 kW/mm² (100 W and 10 μm spot size or 200 W and 20 μm spot size) while short-term experiments have reached 7 MW/mm².⁹ Present commercially available liquid-metal-jet systems are typically based on a Ga/In/Sn alloy, where the emission spectrum is dominated by the 9.25 keV Ga K_α line. For increased penetration through few-cm-thick biological samples, such as a mouse, a new In/Ga liquid-metal-jet source was recently developed.⁷ It has stronger 24 keV (In K_α) line emission and higher efficiency in the bremsstrahlung generation than the Ga/In/Sn source, which improves performance in small-animal imaging.

In the present paper, we demonstrate the first use of liquid-metal-jet sources for whole-body small-animal imaging. The imaging system is demonstrated on mice with high-resolution CT of the skeleton and skeletal details as well as for soft-tissue tumor imaging. The skeletal imaging relies on classical absorption while the soft-tissue imaging exploits the high spatial coherence provided by the source to demonstrate much improved demarcation of tumors using in-line phase contrast.

The skeletal structures can be imaged using classical absorption contrast due to the large natural difference in attenuation coefficient between bone and surrounding tissue. With such high contrast the observable detail is primarily determined by the source spot and the detector properties. Using absorption CT for soft-tissue imaging with high resolution is a much more challenging task due to the inherently poor natural contrast in absorption between different tissue types. Still, small-animal CT is extensively used in small-animal cancer research for, e.g., tumor volume or tumor demarcation studies.¹⁰ For special cases, such as lung tumors, natural contrast may suffice by taking advantage of the considerable difference in attenuation coefficient between air and tissue.¹¹ In general, though, contrast agents are used to increase the absorption of the tumor tissue. Here, however, the maximum reachable contrast is limited by the toxicity of the contrast agent, making observation of small details difficult.

Phase-contrast x-ray imaging has demonstrated substantially improved natural soft-tissue contrast, both using synchrotron¹² and laboratory^{13,14} sources. The most commonly used laboratory-source systems rely on a conventional large-spot source in combination with three gratings, providing high phase sensitivity but source-limited spatial resolution.¹⁵ The method has been applied for tomography,¹⁶ also on soft tissue samples.¹³ The simpler arrangement of the propagation-based in-line method^{17,18} relies on the spatial coherence of the source for contrast and provides high resolution with small-spot sources. The liquid-metal-jet source provides sufficient spatial coherence to allow in-line phase-contrast imaging with high resolution and strong contrast, as has been demonstrated on test objects¹⁹ and for two- and three-dimensional imaging of blood vessels in freshly excised rat kidneys and rat ears.^{20,21} For the blood-vessel tomography, the additional step of phase retrieval is required to obtain a quantitatively correct three-dimensional reconstruction of the object.²² In these experiments, the high resolution and contrast relies on large gas/tissue density differences. In the

present paper, we demonstrate the first sharp demarcation of mm-sized tumors in mice based on natural soft-tissue contrast in in-line laboratory phase-contrast imaging and compare with absorption tomography. Such small tumors have previously only been detected with synchrotron-based phase-contrast systems.²³

II. MATERIALS AND METHODS

Figure 1 illustrates the tomographic imaging arrangement. It consists of the liquid-metal-jet microfocus x-ray source, the object on a rotation stage, and the x-ray detector. The arrangement can be used both for absorption-contrast and phase-contrast imaging, depending on the choice of the source-to-object (R_1) and object-to-detector (R_2) distances. With $R_2 \approx 0$ we have normal absorption imaging, suitable for, e.g., visualization of bone structure. The small x-ray spot of the source reduces the penumbral blurring of the object, which, together with a high-resolution detector, results in detailed images. If the detector is instead positioned some distance behind the object ($R_2 > 0$), the arrangement produces a magnified image of the object on the detector. In addition, our small x-ray spot provides a sufficiently spatially coherent wavefront to produce phase contrast in this in-line arrangement. This gives an additional contrast mechanism, which improves sensitivity in soft-tissue imaging. While the absorption signal depends on changes in the imaginary part of the complex refractive index the in-line phase-contrast signal is dependent on the second derivative of the real part of the complex refractive index.¹⁷

Two different liquid-metal-jet sources were used for the small-animal experiments described here. Both are of the same principal design as outlined in Fig. 1 but circulate different metal alloys. The first is an early version of Excillum's now commercial JXS-D1 (Ref. 9) circulating a Ga/In/Sn alloy (68.5% Ga, 21.5% In, and 10% Sn) with a dominating 9.25 keV Ga K_α emission line. The second is a modified version of the same source, where the alloy was changed to a more indium-rich In/Ga alloy (65% In, 35% Ga). The In/Ga source generates bremsstrahlung more efficiently and has an increased brightness in the 24.2 keV In K_α line compared to the Ga/In/Sn source. Thus, this source generates a larger fraction of higher-energy x-rays, which increases the

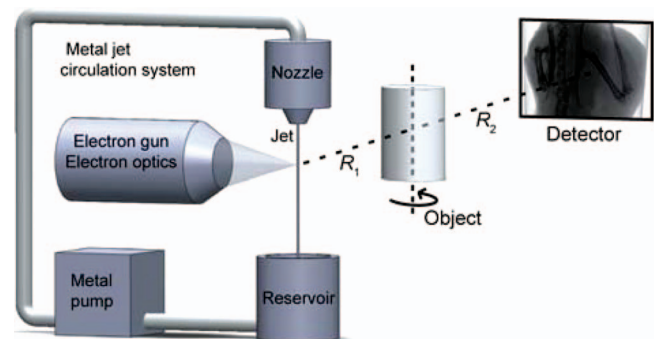


FIG. 1. Experimental arrangement showing the liquid-metal-jet source, the rotatable object, and the detector. The source-to-object distance is R_1 and object-to-detector distance is R_2 .

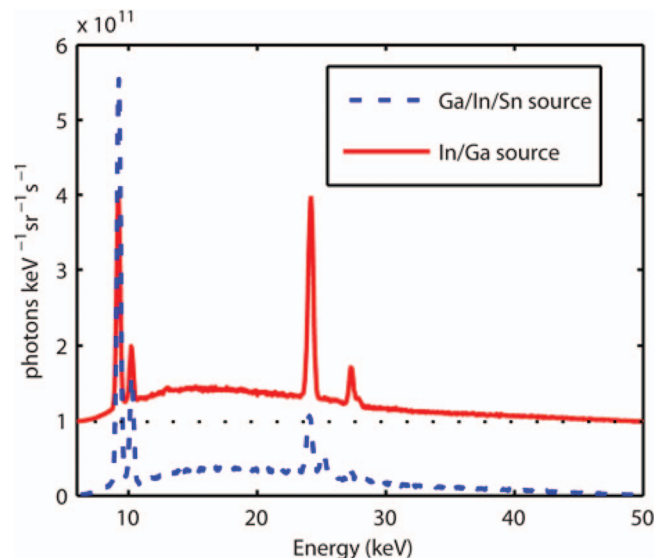


FIG. 2. Quantitative x-ray spectra of the Ga/In/Sn and In/Ga liquid-metal-jet sources, with $7 \mu\text{m}$ FWHM spot size, $200\text{-}\mu\text{m}$ -thick Al filtering and at 50 W e-beam power. The In/Ga spectrum has been shifted upwards.

penetration depth for improved imaging of thicker samples but with the added complication of a heated liquid-metal recirculation system.⁷ Both sources are typically operated at $40\text{--}50 \text{ W}$ electron-beam power with a $7 \mu\text{m}$ full-width at half-maximum (FWHM) x-ray spot. Figure 2 shows the calibrated x-ray spectra of the two sources, filtered with $200\text{-}\mu\text{m}$ -thick Al and measured with a CdTe diode. Both spectra have been normalized to 50 W e-beam power, the power used for the In/Ga/Sn experiments in this paper. The Al filter reduces the radiation dose by removing low-energy photons, which are highly absorbed in thick samples like ours. The Ga/In/Sn source was used to acquire absorption images for the whole-body mouse tomography and for the phase-contrast experiments aimed at finding the boundary between tumorous and healthy soft tissue inside a mouse. The In/Ga source was used for comparative mouse imaging.

In addition to the source, the imaging arrangement consists of a rotatable sample stage for the small-animal (mouse) object and an imaging detector (cf. Fig. 1). The freshly sacrificed mouse was placed in a thin cone-shaped plastic holder, which was fixed in a cylindrical plastic holder on the rotation stage. For ease of lateral alignment, the sample stage also has linear actuators. The detector is a $36 \times 24 \text{ mm}$ water-cooled VHR x-ray camera (Photonic Science). It has a $5 \text{ mg/cm}^2 \text{ Gd}_2\text{O}_2\text{S:Tb}$ scintillator coupled fiber-optically 1:1 to a CCD with $9 \times 9 \mu\text{m}$ pixels. The FWHM of the detector point-spread function is $22 \mu\text{m}$, which was determined from edge-spread-function measurements.

The data acquisition for the tomography was performed by rotating the mouse around a vertical axis (cf. Fig. 1). The recorded projections were flat-field corrected and binned before the three-dimensional image of the mouse was reconstructed with a filtered backprojection algorithm employing cone-beam geometry.²⁴ During the process, tilt angle and center of rotation were manually adjusted for best reconstruction

results. Note that in contrast to Ref. 20, the phase-contrast contribution was relatively small in the present tomography experiments so no phase retrieval was performed on the projections.

For all the present imaging experiments, we used three female mice (Athymic Nude-Foxn1^{nu/nu}, Harlan Laboratories), which were imaged a few hours after they were sacrificed. All animal experiments were carried out in accordance with the Animal Protection Law (SFS 1988:534), the Animal Protection Regulation (SFS 1988:539), and the Regulation for the Swedish National Board for Laboratory Animals (SFS 1988:541) and approved by the Stockholm regional ethics committee for animal research (N358/09).

III. RESULTS AND DISCUSSION

Figure 3 demonstrates high-resolution tomography of the mouse pelvic region. This was performed with the Ga/In/Sn source operating at 50 W with a $6 \times 8 \mu\text{m}^2$ FWHM spot size. A total of 180 projections were acquired over 180° , with $R_1 = 0.49 \text{ m}$, $R_2 = 0.11 \text{ m}$, and 20 s exposure time per projection. A $200\text{-}\mu\text{m}$ -thick Al filter was used to decrease the dose to $5.6 \text{ mGy/projection}$ resulting in a total dose of 1.0 Gy . The dose is calculated from x-ray absorption in 25-mm -thick soft tissue, the approximate diameter of the mouse. Material data are provided by NIST (Ref. 25) and dose rates were verified by ionization-chamber measurements.

Figure 3(a) displays a projection and Fig. 3(c) a reconstructed slice through the pelvic region of the mouse. The vertical position of the slice is shown by the dashed white line in Fig. 3(a). In Fig. 3(b), a closeup of the projection through the knee, indicated by the black rectangle in Fig. 3(a), is presented. A magnification of the slice through the spine and pelvis is shown in Fig. 3(d) while Fig. 3(e) is a magnified image of the knee in Fig. 3(c). The bones of the mouse can be clearly observed in all panels of Fig. 3. This high-resolution imaging also shows the inner bone structure, e.g., in Fig. 3(e), where both the compact outer bone and the trabecular bone is visible. In Fig. 3(e), about $50 \mu\text{m}$ wide details in the trabecular bone can be observed. This result is on the same order as the typical voxel resolution achieved by commercial microfocus sources operating at lower power.^{2,4} Some artifacts due to movement of the mouse during exposure (motion blur) are visible, as for example, indicated by the arrow in Fig. 3(c). Reconstructions based on half the dataset (90 projections over 180° , dose 0.5 Gy) show similar $50\text{-}\mu\text{m}$ detail but with stronger star artifacts due to the lower number of projections, while reconstruction of an extended dataset (360 projections over 180° , dose 2.0 Gy) shows an image similar to that in Fig. 3(c) but with lower noise. The images in Figs. 3(a) and 3(b) have been software binned four times to reduce photon noise. Prior to the filtered backprojection the images in Figs. 3(c)–3(e) have been binned two times. Thus, the pixel size is $36 \times 36 \mu\text{m}$ in Figs. 3(a) and 3(b), and $18 \times 18 \mu\text{m}$ in Figs. 3(c)–3(e). With a magnification of 1.22 , this means that the reconstructed (isotropic) voxel size in the object plane is $30 \mu\text{m}$ in Figs. 3(a) and 3(b), and $15 \mu\text{m}$ in Figs. 3(c)–3(e).

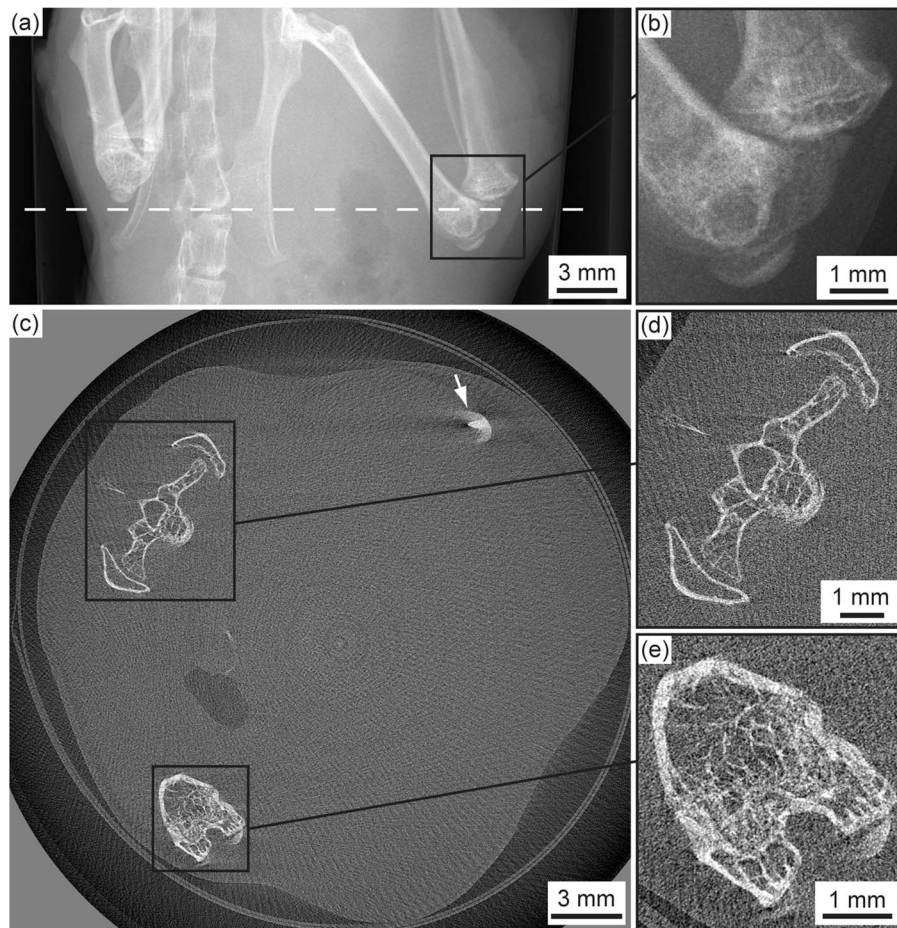


FIG. 3. X-ray imaging and CT of a mouse using the Ga/In/Sn source. (a) A projection image of the mouse pelvic region and (b) a closeup of the knee. (c) The tomographically reconstructed slice through the mouse, where the dashed white line in (a) indicates the position of the slice. Motion blur artifacts are observed as a slight fog at the white arrow. (d) A closeup of the spine and pelvis. (e) A closeup showing $50\ \mu\text{m}$ wide details in the trabecular bone. Distances: $R_1 = 0.49\ \text{m}$ and $R_2 = 0.11\ \text{m}$. Exposure time and dose: (a) and (b) 20 s and 5.6 mGy, (c)–(e) 1 h and 1.0 Gy.

Figure 4 shows an isosurface of the bones in the pelvis region of the mouse. Here, the full tomographic dataset of Fig. 3 has been segmented with respect to local absorption coefficient. The high signal-to-noise ratio allows observations

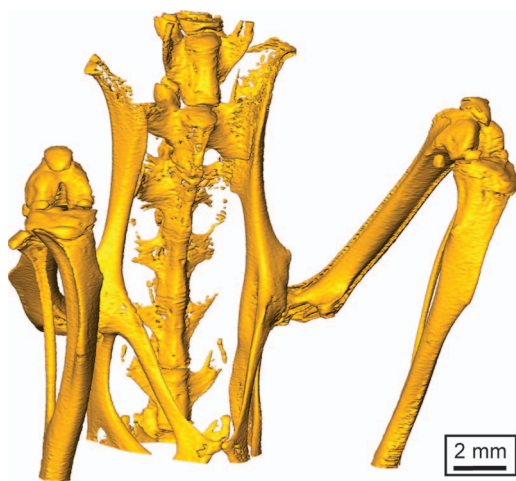


FIG. 4. Segmented and surface-rendered representation of the absorption-CT dataset for the bones in the pelvic region of the nude mouse in Fig. 3.

of, e.g., small details on the bone surface and the structure of the knee.

Figure 5 shows the first small-animal imaging with the higher-photon-energy In/Ga source, showing the abdomen region of the mouse. The source was operating at 40 W with a circular $7\text{-}\mu\text{m}$ -diameter FWHM x-ray spot and $200\text{-}\mu\text{m}$ -thick Al filtering, with $R_1 = 2.4\ \text{m}$ and $R_2 = 0.5\ \text{m}$. Compared to the previous experiment, we have increased the object-to-detector distance (R_2) in order to lower the dose and give a slight phase contrast contribution to the image. The exposure time is 240 s and dose 2.3 mGy. The in-line phase contrast is most clearly observed at the gas bubbles in the abdomen with its characteristic edge enhancement and contributes to a lesser degree to the edge definition of the bones. For future CT experiments, both R_1 and R_2 may be reduced to shorten exposure times. Due to the increased amount of high-energy photons emitted from the In/Ga source (cf. Fig. 2), the same signal-to-noise ratio may be obtained with a reduced exposure time, compared to the Ga/In/Sn source. This also means that for a constant signal-to-noise ratio, the dose delivered to the mouse can be decreased by using the In/Ga source, which is beneficial for biomedical imaging of live animals.



FIG. 5. X-ray projection image of a mouse, using the new In/Ga liquid-metal-jet x-ray source. The distances $R_1 = 2.4$ m and $R_2 = 0.5$ m results in a phase-contrast contribution to the image. Exposure time and dose: 240 s and 2.3 mGy.

In Fig. 6, we investigate the method's potential for soft-tissue tumor demarcation in whole mouse. In order to induce tumor formation, 1×10^6 E1A/Ras-transformed mouse embryonic fibroblasts were injected under the skin of the mouse. After approximately four weeks, the tumor had reached a size of a few mm and the mouse was sacrificed and imaged with the Ga/In/Sn source. The source was operating at 50 W with a circular $7\text{-}\mu\text{m}$ -diameter FWHM x-ray spot and $200\text{-}\mu\text{m}$ -thick Al filtering. Figure 6(a) shows an in-line phase-contrast projection image of the tumor region. The distances are $R_1 = 1$ m and $R_2 = 2$ m, exposure time 300 s, and dose 19 mGy. The tumor (T) is located to the right and the surrounding fat tissue (F) and the thigh bone (B) are seen on the left. Note that contrary to in the absorption imaging in Figs. 3 and 5, we have chosen to keep the original contrast, i.e., the bone is

black, in this phase image for proper evaluation of the soft-tissue phase contrast. The black arrows indicate the position of the edge between the tumor and the healthy tissue, showing distinct edge enhancement due to phase contrast. The strong edge contrast is due to the long propagation distance (R_2) in combination with the tumor being partially surrounded by fat tissue, which has lower density than the tumor. This density gradient is the major reason for the large difference in complex refractive index at the tumor boundary leading to a large in-line phase-contrast signal. The absorption signal from the tumor interface in Fig. 6(a) is, however, relatively weak, which can be realized by comparing pixel values on opposite sides of the tumor edge.

For comparison, the same mouse tumor was tomographically imaged in a similar manner as in Fig. 3 to produce an absorption-contrast image, cf. Fig. 6(b). The source was running at 50 W, with a spot size of $7\ \mu\text{m}$, and $200\text{-}\mu\text{m}$ -thick Al filtering. A total of 180 projections were recorded over 180° , with $R_1 = 0.385$ m and $R_2 = 0.115$ m. For these distances, the amount of phase contrast is negligible. The exposure time is 15 s/projection and the dose is 1.3 Gy. The position of the reconstructed slice is indicated by the dashed white line in Fig. 6(a). The bones are white, the cone-shaped plastic holder is visible around the mouse, and the black areas are air. The tumor (T) is situated just beneath the skin of the mouse, which bulges slightly outwards into the surrounding air. Again, the black arrows indicate the position of the tumor edge. Here, it is the difference in attenuation coefficient between the tumor and the fat tissue that makes tumor demarcation possible, albeit not with the same distinction as in the single phase-contrast image. Furthermore, the total dose of the absorption dataset is 1.3 Gy, as compared to the 19 mGy in the phase-contrast image. Reconstructing half the dataset (90 projections over 180° , dose 0.66 Gy) yields images that do not allow complete demarcation of the tumor,

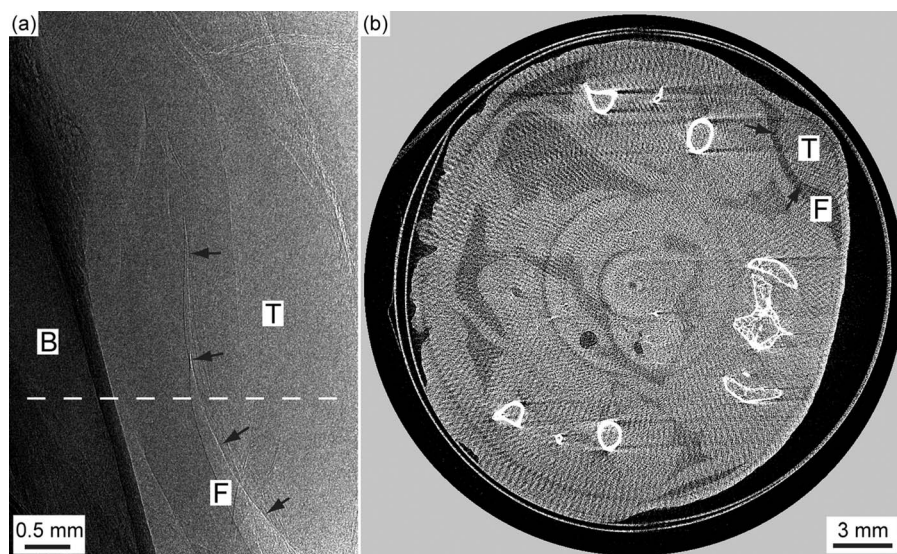


FIG. 6. (a) X-ray phase-contrast image of a mouse tumor. The black arrows indicate the position of the boundary between the tumor (T) and surrounding fat tissue (F). The dark areas are bone (B). (b) Absorption CT of the same mouse. The slice corresponds to the position of the dashed white line in (a) and the arrows point at the same tumor interface as in (a). Ga/In/Sn source. Distances: (a) $R_1 = 1$ m and $R_2 = 2$ m, (b) $R_1 = 0.385$ m, and $R_2 = 0.115$ m. Exposure time and dose: (a) 300 s and 19 mGy, (b) 45 min and 1.3 Gy.

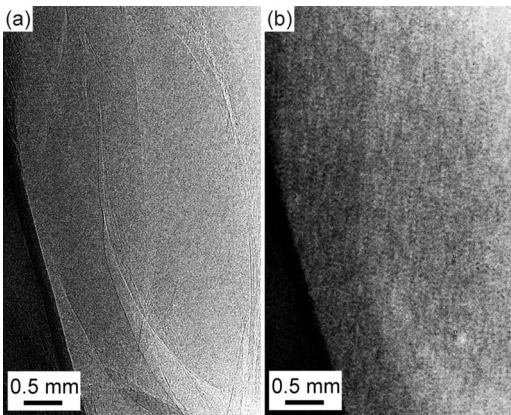


FIG. 7. Comparison between phase-contrast and absorption-contrast tumor imaging at approximately the same dose. (a) Part of the Fig. 6(a) phase-contrast image at 19 mGy. (b) Same area in absorption at 15 mGy. Ga/In/Sn source. Distances: (a) $R_1 = 1$ m and $R_2 = 2$ m, (b) $R_1 = 0.385$ m, and $R_2 = 0.115$ m. Exposure time: (a) 300 s, (b) 30 s.

due to too high photon noise. Finally, we compare absorption imaging and phase-contrast imaging with approximately the same dose in Fig. 7. Figure 7(a) is the central part of Fig. 6(a) (dose 19 mGy) while Fig. 7(b) shows the same area in absorption contrast. In Fig. 7(b), we have added two opposite projections, acquired with $R_1 = 0.385$ m and $R_2 = 0.115$ m, for a total dose of 15 mGy. The phase-contrast image clearly provides superior demarcation. This improvement in tumor demarcation may be further investigated by acquiring a full phase-contrast CT dataset to compare with absorption CT. However, a full quantitative comparison would require an extensive investigation of factors such as imaging distances, exposure time, and phase-retrieval parameters, and will thus be left to future work.

It is clear that in-line phase contrast shows promise for improved natural-contrast tumor demarcation at low dose. However, we also note that the applicability of the method depends on many parameters. In the present case, the sharp edge enhancement observed in the phase images [Figs. 6(a) and 7(a)], as well as the relatively high contrast in the absorption CT [Fig. 6(b)], are due to the tumor being surrounded by fat tissue. The two tissue types have different densities and thereby different complex refractive indices. However, when the tumor is in contact with surrounding tissue with almost identical index of refraction the edge of the tumor cannot be detected with phase contrast. This is observed in Fig. 6(a) in the area above the black arrows. Similarly, it is not possible to tell the difference between tumor and muscle tissue in the natural-contrast absorption image of Fig. 6(b) since the difference in x-ray mass attenuation coefficient of the two tissue types is too small. Still, the experiments demonstrate that in-line phase contrast using the liquid-metal-jet source clearly provides an additional contrast mechanism in addition to absorption, which may be exploited for improved tumor demarcation and other soft-tissue imaging applications in suitable cases.

IV. CONCLUSIONS

We have demonstrated the first application of liquid-metal-jet microfocus sources for small-animal x-ray imaging, using both absorption and phase contrast. The source properties such as spot size and spectrum are found appropriate for small-animal-sized biological objects and reconstructions demonstrate the method's applicability for high-resolution absorption CT. In addition, we exploit the high spatial coherence to demonstrate the first phase-contrast-assisted tumor demarcation in a mouse with a laboratory-source system. The phase contrast is observed to greatly improve the detectability of the tumor edge in a projection image, compared to conventional absorption contrast. Such few-mm-sized tumors have previously only been visualized with a synchrotron-source-based phase-contrast system²³ while laboratory-source-based systems have been restricted to tumor sizes of a few tens of mm¹⁴ which renders them less suitable for small-animal research.

The dose delivered to the mouse in the phase-contrast experiment (19 mGy) is already low for small-animal imaging. However, the doses in the absorption-tomography experiments described in this paper were about a factor of 2 higher than doses commonly used in small-animal imaging.⁴ The dose may be further reduced in future experiments depending on the specific image task and the features that need to be detected. The dose and exposure time can also be reduced by the use of a detector more suitable for small-animal imaging, i.e., one with higher absorption efficiency in the 20–25 keV energy range. Our present detector is optimized for low-energy (9 keV) x-rays, having a scintillator absorption efficiency of only 11% at 25 keV.

Finally, we note that exposure times for the absorption-imaging experiments are in the same range as those obtained with existing sources, while relatively long for the phase-contrast imaging. Fortunately, the liquid-metal-jet arrangement does not have the same basic thermal power-loading limitation as conventional microfocus x-ray sources. In the next few years, we can expect liquid-metal-jet sources with up to ten times higher power without an increase in spot size. Thus, there appears to be potential for a considerable reduction in exposure time without sacrificing image quality.

ACKNOWLEDGMENTS

The authors thank Per Takman, Richard Tjörnhammar, and Peter Skoglund for early contributions and Margareta Wilhelm for supplying the tumor cells. This work was supported by the Swedish Research Council, the Swedish Governmental Agency for Innovation Systems, and the Wallenberg Foundation.

^{a)} Author to whom correspondence should be addressed. Electronic mail: daniel.larsson@biox.kth.se

¹ G. C. Kagadis, G. Loudos, K. Katsanos, S. G. Langer, and G. C. Nikiforidis, "In vivo small animal imaging: Current status and future prospects," *Med. Phys.* **37**, 6421–6442 (2010).

² S. J. Schambach, S. Bag, L. Schilling, C. Groden, and M. A. Brockmann, "Application of micro-CT in small animal imaging," *Methods* **50**, 2–13 (2010).

- ³M. J. Paulus, S. S. Gleason, S. J. Kennel, P. R. Hunsicker, and D. K. Johnson, "High resolution X-ray computed tomography: An emerging tool for small animal cancer research," *Neoplasia* **2**, 62–70 (2000).
- ⁴C. T. Badea, M. Drangova, D. W. Holdsworth, and G. A. Johnson, "*In vivo* small-animal imaging using micro-CT and digital subtraction angiography," *Phys. Med. Biol.* **53**, R319–R350 (2008).
- ⁵O. Hemberg, M. Otendal, and H. M. Hertz, "Liquid-metal-jet anode electron-impact x-ray source," *Appl. Phys. Lett.* **83**, 1483–1485 (2003).
- ⁶M. Otendal, T. Tuohimaa, U. Vogt, and H. M. Hertz, "A 9 keV electron-impact liquid-gallium-jet x-ray source," *Rev. Sci. Instrum.* **79**, 016102 (2008).
- ⁷D. H. Larsson, P. A. C. Takman, U. Lundstrom, A. Burvall, and H. M. Hertz, "A 24 keV liquid-metal-jet x-ray source for biomedical applications," *Rev. Sci. Instrum.* **82**, 123701 (2011).
- ⁸D. E. Grider, A. Wright, and P. K. Ausburn, "Electron-beam melting in microfocus X-ray tubes," *J. Phys. D* **19**, 2281–2292 (1986).
- ⁹<http://www.excillum.com>.
- ¹⁰S. M. Weber, K. A. Peterson, B. Durkee, Q. Chen, M. Longino, T. Warner, F. T. Lee, and J. P. Weichert, "Imaging of murine liver tumor using MicroCT with a hepatocyte-selective contrast agent: Accuracy is dependent on adequate contrast enhancement," *J. Surg. Res.* **119**, 41–45 (2004).
- ¹¹Y. Hori, N. Takasuka, M. Mutoh, T. Kitahashi, S. Kojima, K. Imaida, M. Suzuki, K. Kohara, S. Yamamoto, N. Moriyama, T. Sugimura, and K. Wakabayashi, "Periodic analysis of urethane-induced pulmonary tumors in living A/J mice by respiration-gated X-ray microcomputed tomography," *Cancer Sci.* **99**, 1774–1777 (2008).
- ¹²R. A. Lewis, "Medical phase contrast x-ray imaging: Current status and future prospects," *Phys. Med. Biol.* **49**, 3573–3583 (2004).
- ¹³M. Bech, T. H. Jensen, R. Feidenhans'l, O. Bunk, C. David, and F. Pfeiffer, "Soft-tissue phase-contrast tomography with an x-ray tube source," *Phys. Med. Biol.* **54**, 2747–2753 (2009).
- ¹⁴M. Stampanoni, Z. T. Wang, T. Thuring, C. David, E. Roessl, M. Trippel, R. A. Kubik-Huch, G. Singer, M. K. Hohl, and N. Hauser, "The first analysis and clinical evaluation of native breast tissue using differential phase-contrast mammography," *Invest. Radiol.* **46**, 801–806 (2011).
- ¹⁵F. Pfeiffer, T. Weitkamp, O. Bunk, and C. David, "Phase retrieval and differential phase-contrast imaging with low-brilliance X-ray sources," *Nat. Phys.* **2**, 258–261 (2006).
- ¹⁶F. Pfeiffer, C. Kottler, O. Bunk, and C. David, "Hard X-ray phase tomography with low-brilliance sources," *Phys. Rev. Lett.* **98**, 108105 (2007).
- ¹⁷S. W. Wilkins, T. E. Gureyev, D. Gao, A. Pogany, and A. W. Stevenson, "Phase-contrast imaging using polychromatic hard X-rays," *Nature (London)* **384**, 335–338 (1996).
- ¹⁸S. C. Mayo, P. R. Miller, S. W. Wilkins, T. J. Davis, D. Gao, T. E. Gureyev, D. Paganin, D. J. Parry, A. Pogany, and A. W. Stevenson, "Quantitative X-ray projection microscopy: Phase-contrast and multi-spectral imaging," *J. Microsc.* **207**, 79–96 (2002).
- ¹⁹T. Tuohimaa, M. Otendal, and H. M. Hertz, "Phase-contrast x-ray imaging with a liquid-metal-jet-anode microfocus source," *Appl. Phys. Lett.* **91**, 074104 (2007).
- ²⁰U. Lundström, D. H. Larsson, A. Burvall, P. A. C. Takman, L. Scott, H. Brismar, and H. M. Hertz, "X-ray phase contrast for CO₂ microangiography," *Phys. Med. Biol.* **57**, 2603–2617 (2012).
- ²¹U. Lundström, D. H. Larsson, A. Burvall, L. Scott, U. K. Westermark, M. Wilhelm, M. Arsenian Henriksson, and H. M. Hertz, "X-ray phase-contrast CO₂ angiography for sub-10- μ m-vessel imaging," *Phys. Med. Biol.* **57**, 7431–7441 (2012).
- ²²A. Burvall, U. Lundström, P. A. C. Takman, D. H. Larsson, and H. M. Hertz, "Phase retrieval in X-ray phase-contrast imaging suitable for tomography," *Opt. Express* **19**, 10359–10376 (2011).
- ²³F. Pfeiffer, O. Bunk, C. David, M. Bech, G. Le Duc, A. Bravin, and P. Cloetens, "High-resolution brain tumor visualization using three-dimensional x-ray phase contrast tomography," *Phys. Med. Biol.* **52**, 6923–6930 (2007).
- ²⁴J. Vlassenbroeck, M. Dierick, B. Masschaele, V. Cnudde, L. Van Hoorebeke, and P. Jacobs, "Software tools for quantification of X-ray microtomography at the UGCT," *Nucl. Instrum. Methods Phys. Res. A* **580**, 442–445 (2007).
- ²⁵J. H. Hubbell and S. M. Seltzer, "Tables of x-ray mass attenuation coefficients and mass energy-absorption coefficients from 1 keV to 20 MeV for elements Z = 1 to 92 and 48 additional substances of dosimetric interest," 2011 (available URL: <http://www.nist.gov/pml/data/xraycoef/index.cfm>).